

# HIGH-PRECISION CAPTURING AND AI INSPECTION SYSTEM FOR DETECTING ANOMALIES IN PEMFC MEAS

In Joo<sup>1</sup>, Kyeongtae Son<sup>2</sup>, Yong-Seong Kim<sup>2</sup>, Ga-Ae Ryu<sup>3</sup> and Kwan-Hee Yoo<sup>1,\*</sup>

<sup>1</sup>Department of Computer Science, Chungbuk National University, Cheongju City, Republic of Korea

<sup>2</sup>LAT Co.,Ltd, Suwon City, Gyeonggi-do, Republic of Korea

<sup>3</sup>Hydrogen Digital Convergence Center, Korea Institute of Ceramic Engineering & Technology, Jinju City, Republic of Korea

## ABSTRACT

*Membrane Electrode Assembly (MEA) quality strongly affects performance and yield in proton exchange membrane fuel cell (PEMFC) manufacturing. This paper presents an end-to-end, production-oriented inspection system that automates MEA feeding, dual-side high-resolution line-scan imaging, and AI-based surface defect decision making. The system accepts 3-/5-layer MEA sheets stacked with interleaving papers in a loader tray, performs separator removal and vacuum fixation, then scans the MEA with coaxial and side lighting to acquire uniform, distortion-free high resolution 8192×11000 images. A hybrid AI model integrates EfficientNetV2-based classification with DETR-based object detection; a quadrant tiling strategy and bilateral-filter+CLAHE preprocessing enable stable inference on the high-resolution images under GPU memory constraints. Evaluation of our system achieved 97.11% accuracy and 39.2 s/part tact time for dual-side inspection.*

## KEYWORDS

*MEA, line-scan imaging, automated handling, vacuum pick-up, deep learning, EfficientNetV2, DETR, anomaly detection*

## 1. INTRODUCTION

Proton exchange membrane fuel cells (PEMFCs) are moving beyond early demonstrations and are increasingly deployed in mobility and stationary power applications, driven by their high power density and low local emissions [1]. As deployment scales, commercialization pressure shifts from single-cell performance toward manufacturability, cost reduction, and durability assurance under mass-production conditions. In this context, the membrane electrode assembly (MEA)—the core electrochemical component—remains a major contributor to stack cost and a primary driver of performance variability, making stable MEA manufacturing and quality control (QC) central to competitive PEMFC production [2,3]. Recent manufacturing-focused studies further report that production-induced MEA irregularities can measurably degrade performance and complicate diagnosis, reinforcing the need for systematic QC technologies suitable for factory environments [4].

Scaling MEA production introduces two conflicting QC requirements: throughput compatible with shop-floor takt time and reliable detection of subtle, intermittent, or low-contrast defects that can shorten lifetime or reduce stack efficiency [4]. This problem is amplified by the physical characteristics of MEA sheets: they are thin, compliant, and vulnerable to handling-induced deformation; inspection often spans large areas (hundreds of millimeters in scan length) and frequently requires front/back evaluation. Consequently, conventional visual inspection—manual or semi-automated—tends to be labor-intensive, operator-dependent, and inconsistent when defects are small, ambiguous, or sporadic, motivating a transition toward repeatable imaging and data-driven inspection [4,5].

In practical production, typical MEA surface and handling anomalies include scratches, foreign particles, dents, pinholes, folds/wrinkles, and discoloration. Such defects may originate from coating/lamination, cutting, interleaf separation, transfer, or temporary storage, and may appear sparsely and locally. Therefore, a deployable MEA inspection approach must first ensure mechanical stability and optical consistency—because model robustness is strongly constrained by imaging repeatability—then apply reliable artificial intelligence (AI) decision-making that can generalize across shifts and lots without frequent re-labeling. This manufacturing-grounded view aligns with the broader trend of automation technologies for MEA production and inspection, where stable material handling and consistent measurement conditions are prerequisites for scalable QC [5].

This paper proposes a practical inspection system for PEMFC MEA sheets that integrates an automated capturing system for delicate handling and repeatable high-resolution imaging, and an AI inspection system for defect classification and localization of anomalies within a closed-loop production sequence. The capturing system couples an automated input device (loader) with a precision scanning stage and line-scan imaging to provide large-area, high-resolution inspection under controlled illumination. In the reported verification, the system demonstrated inspection performance compatible with shop-floor operation, including micro-level motion repeatability and cycle-time feasibility, supporting stable registration and consistent learning/inference across repeated runs.

On the AI side, the inspection pipeline follows a three-stage strategy that mirrors shop-floor decision needs: preprocessing of the high-resolution image, defect-type classification to support diagnosis and process feedback, and detection/localization to support reject logic and defect mapping. The pipeline leverages established computer-vision preprocessing and enhancement (e.g., contrast-limited adaptive histogram equalization (CLAHE) [6], and morphology-based operations [7]) grounded in standard vision practice [8]. For learning-based inspection, modern deep vision methods provide complementary advantages: efficient convolutional backbones enable fast, accurate classification (e.g., EfficientNetV2 [9], building on the evolution of CNN-based recognition [10,11]), while transformer-based detectors support end-to-end set prediction for localization without heavy post-processing (e.g., DETR [12]). Region-proposal-based detection remains a useful reference point for industrial localization pipelines (e.g., Faster R-CNN [13]), and large-scale detection benchmarks have shaped standard evaluation and training protocols for object localization tasks [14]. From an implementation standpoint, the optimization of large-scale machine learning systems and training stability is supported by well-established methods in modern optimization literature [15].

Rather than proposing a new model architecture in isolation, this work contributes a production-grounded, system-level consolidation of MEA inspection practice based on an industrial verification report. Specifically, we provide:

- an integrated capture–inspection architecture (loader + precision scan stage + line-scan imaging + AI stack) designed around end-to-end stability for thin-film MEAs;
- an MEA-focused defect taxonomy and dataset construction procedure aligned with factory traceability requirements;
- a practical classification–detection pipeline reflecting modern vision practice (CNN-based classification [9,10], transformer-based localization [12], with conventional vision preprocessing [6,7,8]); and
- shop-floor evaluation metrics that are directly interpretable for deployment, including takt time, non-detection rate, accuracy, and motion repeatability, emphasizing operational performance beyond offline accuracy alone.

The remainder of the paper is organized as follows. Section 2 describes the overall system architecture, including the capture subsystem and the AI inspection workflow. Subsequent sections present experimental protocols, evaluation results with production-relevant metrics, discussion of representative failure cases and practical considerations, and concluding remarks on scaling MEA QC for mass production.

## 2. THE PROPOSED SYSTEM

### 2.1. System Overview

An MEA is a large-area, film-like component composed of stacked electrode, gasket, and membrane layers. During manufacturing, anomalies such as foreign particles, folds/wrinkles, pinholes and electrode–gasket misalignment (eccentricity) may occur, which directly affect PEMFC performance and lifetime. In mass production, an inspection platform must simultaneously satisfy: short takt time, sufficient spatial resolution for micro-defects, repeatable handling/alignment, and traceability of results (history and statistics). To meet these requirements, we design the capturing system and the AI inspection system as separable modules and couple them through a three-layer interface (trigger–data–result) to realize inline quality control as shown in Figure 1. The capturing system (Fig. 1(a)) is responsible for product handling/transfer and imaging quality assurance, while the AI inspection system (Fig. 1(b)) provides anomaly decision-making, visualization, database logging, and process feedback.

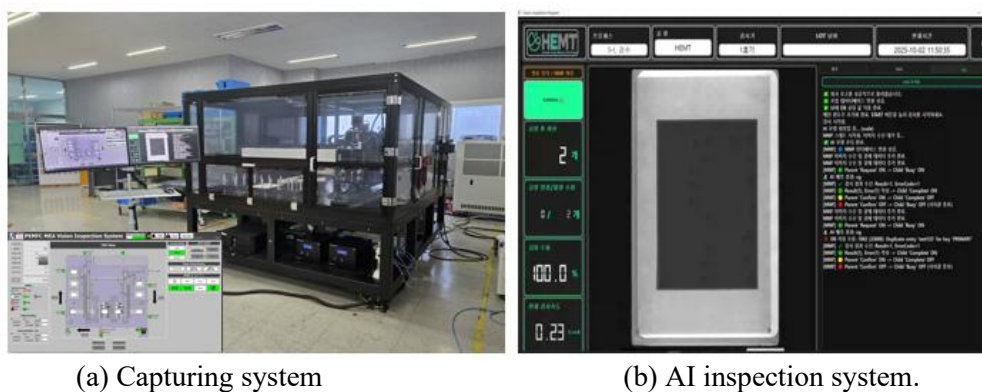


Figure 1. Overview of the proposed system

### 2.2. The Capturing System

The capturing system aims to stably generate inspection-grade images while satisfying the required production and geometric specifications. The proposed capturing system meets an

inspection limit of  $30.72 \mu\text{m}$ , a takt time of 15.6 sec per MEA, and a stage positioning repeatability of  $\pm 7.67 \mu\text{m}$ , ensuring both throughput and high image consistency for downstream AI-based anomaly detection.

The capturing system is composed of a handling module and an optics module. The handling module includes a loader/unloader with interleaf separation, vacuum pick-up transfer, and an inspection stage. Starting from a tray stacked as interleaf/MEA/interleaf, the interleaf sheet is removed first, and the MEA is transferred to the inspection stage where it is fixed by vacuum suction. After coaxial and side-illumination imaging, the system waits for the AI decision; conforming samples are routed to the OK unloader, and nonconforming samples are routed to the NG unloader. Interleaf sheets are re-stacked on top of the product to maintain continuity in the downstream process. For 5-layer MEA products, an initial design used a two-zone vacuum stage to separate electrode and gasket regions; however, grooves on the stage introduced image artifacts, complicating labeling and model learning. Therefore, the stage was redesigned as a flat suction stage without grooves to eliminate optical interference. In addition, excessive vacuum force can deform thin-film MEAs; thus, the pneumatic line was modified and the vacuum level was reduced from  $-69 \text{ kPa}$  to  $-10 \text{ kPa}$  to prevent mechanical deformation while maintaining stable fixation.

To verify the mechanical stability required for inspection-grade imaging, we evaluated the positioning repeatability of the inspection stage by repeatedly moving the stage to predetermined coordinates 10 times and measuring the resulting positional deviations. As shown in Figure 2 (LMAC tuning and repeatability evaluation), after controller tuning, the capturing stage achieved a repeatability of  $\pm 7.67 \mu\text{m}$  across repeated motions, confirming that the handling/positioning module satisfies the precision requirement for consistent line-scan acquisition and reliable defect localization.

no	X	Y	no	X	Y	no	X	Y
1	1895.03	1603.54	1	12500.70	3721.14	1	1443.14	1268.53
2	1894.97	1603.46	2	12500.83	3720.53	2	1443.17	1268.53
3	1895.14	1603.77	3	12500.42	3721.37	3	1443.11	1268.59
4	1895.10	1603.51	4	12500.95	3721.83	4	1443.20	1268.70
5	1895.32	1604.30	5	12500.73	3721.48	5	1443.08	1268.42
6	1895.20	1603.50	6	12500.53	3721.65	6	1443.16	1268.73
7	1895.29	1603.56	7	12500.84	3721.37	7	1443.17	1268.36
8	1895.05	1603.40	8	12500.63	3720.31	8	1443.12	1268.54
9	1895.16	1603.28	9	12500.39	3721.26	9	1443.13	1268.86
10	1895.18	1604.15	10	12500.30	3721.54	10	1443.14	1268.75

Figure 2. Stage positioning repeatability evaluation and LMAC tuning results for the capturing system. The stage was moved to predefined positions repeatedly (10 cycles), and the positional deviation in X/Y directions confirms a repeatability of  $\pm 7.67 \mu\text{m}$ .

The optics module consists of a line-scan camera, lens, and illumination. Because line-scan imaging is sensitive to axis alignment, tilt, and vibration, the camera's vertical/horizontal alignment and working distance were precisely adjusted. Both coaxial and side illumination were applied; the side-lighting angle was set to  $30^\circ$  relative to the stage. Considering the product size, the scan travel was configured to 330 mm and start/end positions were calibrated per illumination condition to obtain uniform irradiance and sharp focus without distortion.

Captured data are stored as high-resolution images ( $8192 \times 11000$ ) together with metadata such as product information, illumination condition, recipe (exposure/speed/light intensity), and timestamp. After the capturing finishing signal, the AI inspection system gets the corresponding memory address and performs inference. Two representative raw images captured by the proposed system (one under coaxial illumination and one under side illumination) are also presented as sample inputs to demonstrate the inspection-grade image quality.

### 2.3. Anomaly Inspection System based on AI

Figure 3 illustrates the proposed AI-based inspection system for detecting anomalies in PEMFC MEAs. The system is organized as a three-stage pipeline: preprocessing, anomaly classification, and anomaly detection. This modular structure is designed to satisfy two practical requirements in inline manufacturing: producing stable decisions under real-world imaging variability and providing interpretable evidence (location/type) for quality assurance and process feedback. Accordingly, the pipeline first normalizes the image appearance, then performs fast screening, and finally localizes defects when necessary.

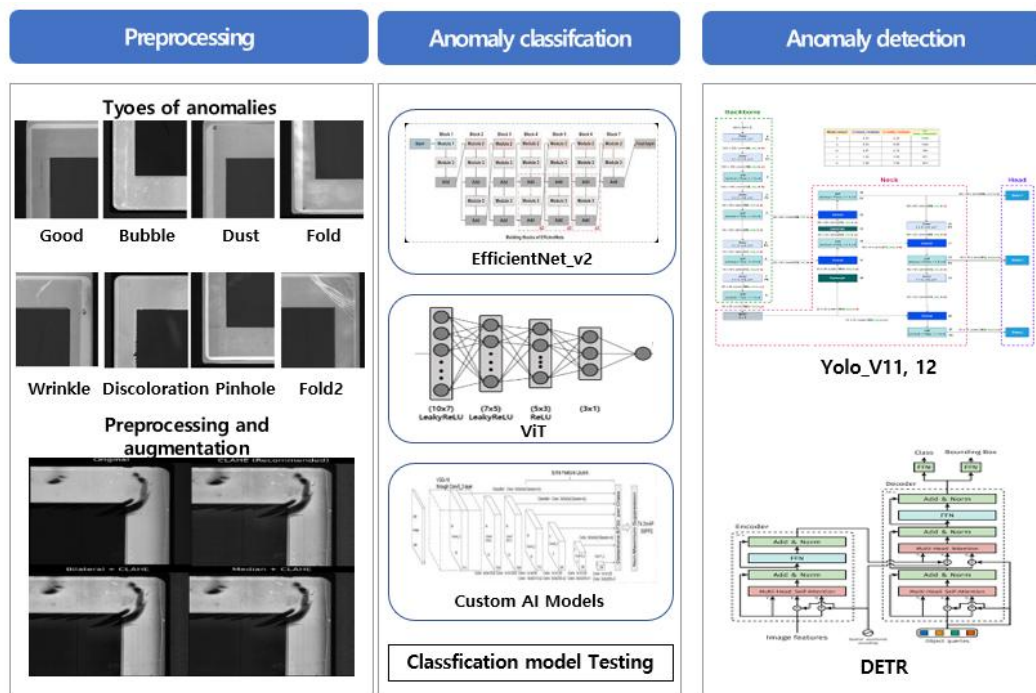


Figure 3. AI-based MEA inspection workflow: preprocessing/augmentation, anomaly classification and anomaly detection.

In this study, the surface and geometric anomalies observed in PEMFC MEA production were organized into region-based defect categories, as summarized in Table 1. Because an MEA consists of multiple functional regions, including the gasket, the electrode (active layer), and their relative alignment, defects can be most effectively defined according to their occurrence region and manifestation pattern. This classification reflects the physical structure of the MEA and provides a practical basis for establishing consistent inspection criteria and interpretable decision-making.

As shown in Table 1, MEA defects exhibit several important characteristics. Gasket defects, such as bubbles and folds/creases, mainly appear as area-level irregularities in the sealing region, whereas electrode defects, including wrinkles/folds, discoloration, and pinholes, are typically localized anomalies that may affect electrochemical performance and durability. In addition, many defects are subject to strict geometric acceptance criteria, such as allowable size, area, or occurrence count, requiring the inspection system to detect small, sparse, and low-contrast

defects while supporting quantitative pass/fail decisions. In contrast, alignment eccentricity is a geometry-based defect defined by positional deviation between the electrode and gasket. Therefore, the defect categories in Table 1 define the inspection scope of this study and highlight the need for an inspection framework that can address both appearance-based and geometry-based anomalies under tight dimensional tolerances.

Table 1. Defect taxonomy and model assignment for PEMFC MEA inspection.

No.	Region	Defect type	Acceptance criterion	Method
1	Gasket	Bubble	< 3 mm×3 mm, <1	Classification
2	Gasket	Fold/Crease	< 3 mm×3 mm, <1	Classification
3	Electrode/Gasket	Particle/Contamination	< 0.4 mm×0.4 mm, <1	Detection
4	Electrode	Wrinkle/Fold	Area < 1/10 mm, <2	Detection
5	Electrode	Discoloration	< 0.4 mm×0.4 mm, <1	Detection
6	Electrode	Pinhole	< 0.4 mm×0.4 mm, <1	Detection
7	Alignment	Eccentricity	Active layer 2 mm ± 1 mm	Image proc.

In preprocessing, contrast-limited adaptive histogram equalization (CLAHE), Median+CLAHE, and Bilateral+CLAHE were compared for contrast enhancement and noise reduction. On the validation set, Bilateral+CLAHE achieved the best accuracy (0.892473) and was adopted. Direct inference on the full-resolution 8192×11000 image increases GPU memory usage and latency; therefore, the image is partitioned into four quadrants and inspected independently. This strategy mitigates feature dilution for micro-defects and distributes computation into smaller sub-problems, improving both stability and speed. During training, moderate augmentation (small translations/rotations and mild brightness–contrast perturbations within operational ranges) is applied to improve generalization, while avoiding unrealistic artifact generation that could bias the classifier.

The classification stage provides rapid sample-level screening and outputs the predicted category (good vs. anomaly type) with confidence scores. As illustrated in Figure 3, the system supports multiple classification backbones, including EfficientNetV2, Vision Transformer (ViT), and custom AI models, enabling flexible trade-offs between accuracy and throughput. In our study, classification can operate as an early-exit mechanism: high-confidence “good” samples may bypass detection to minimize processing time, whereas anomalous or low-confidence cases trigger the detection module for localization and verification. When region-wise inference is used, the classifier produces per-region probabilities that can be fused using conservative rules (e.g., “any-anomaly” voting), which is suitable for quality control because a single localized defect is sufficient to reject a part.

The detection stage produces spatially explicit results for explainability and process feedback. The system integrates real-time detectors such as YOLO (v11/v12) and transformer-based detectors such as DETR, each providing bounding boxes, class labels, and confidence scores. In practice, lightweight YOLO variants are favorable for high-throughput inline operation, while DETR can serve as an alternative when attention-based global reasoning improves detection stability for certain defect modes. Detection outputs are visualized as overlays on the captured image and are logged with metadata to support traceability (lot-wise statistics, defect hotspots, and long-term monitoring). The final inspection decision is then returned to the manufacturing controller with defect descriptors (type and location), enabling automated routing and consistent quality assurance.

### 2.3. Integrated System

As mentioned earlier, the capturing system minimizes variation in illumination, alignment, suction, and vibration to produce inspection-grade line-scan images, while the AI inspection system provides real-time decisions, defect localization, and traceable records via preprocessing, quadrant-based inference, and combined classification/detection/eccentricity analysis. By coupling the two subsystems through trigger–data–result interfaces, the proposed platform achieves both high throughput and reliable anomaly detection for inline PEMFC MEA quality control. To support shop-floor operation, the AI pipeline is wrapped in a GUI-based vision inspection application designed as a three-layer architecture: a user interface layer for image preview, mode selection, real-time visualization, and log filtering; an inference engine layer containing preprocessing, EfficientNetV2 classification, DETR detection, and result fusion; and a data management layer that stores inspection history and synchronizes results with a database. The system allows operators to switch between classification-only and detection-enabled inspection depending on the production scenario, while maintaining traceability for continuous improvement and audit readiness.

### 3. EXPERIMENTAL METRICS AND RESULTS

#### 3.1. Evaluation Metrics of Capturing System

In this paper, we evaluated the capturing system (Loader–Stage–Imaging–Unloader) using four metrics: throughput time, handling reliability (breakage rate), stage positioning repeatability, and minimum detectable feature size. Throughput time was defined as one full cycle from Loader input to Unloader output for a single MEA; cycle times were recorded over repeated runs and averaged (s/ea). Breakage rate was measured by repeatedly transporting MEA sheets and counting physically damaged samples (e.g., tear, fold, scratch, edge damage). The breakage rate (Eq. (1)) was computed as

$$\text{Breakage rate (\%)} = \frac{\text{\#damaged sheets}}{N_{\text{sheets}} \times N_{\text{cycles}}} \times 100. \quad (1)$$

Positioning repeatability was evaluated by commanding the inspection stage to the same predefined position 10 times and measuring the return-position deviation ( $\mu\text{m}$ ). Minimum detectable feature size was determined via pixel-to-length calibration and measurement of the smallest resolvable micro-scale target (or artificial micro-defect) under the same imaging conditions.

#### 3.2. Evaluation Metrics of AI Inspection System

To evaluate the AI inspection model, we report classification accuracy and the non-detection rate on OK samples, i.e., the false reject rate (FRR) that directly impacts production yield. For a binary decision (OK vs. NG), the outcomes are defined as follows: TP (true positive) denotes the number of NG samples correctly predicted as NG; TN (true negative) denotes the number of OK samples correctly predicted as OK; FP (false positive) denotes the number of OK samples incorrectly predicted as NG (false reject); and FN (false negative) denotes the number of NG samples incorrectly predicted as OK (false accept). Based on these definitions, accuracy (Eq. (2)) is computed as the fraction of correct predictions:

$$\text{Accuracy} = \frac{TP + TN}{TP + TN + FP + FN}. \quad (2)$$

In addition, to explicitly quantify unintended rejection of good products, we compute the non-detection rate on OK (FRR) (Eq. (3)) as:

$$\text{FRR} = \frac{FP}{TN + FP} \times 100\%. \quad (3)$$

where TN+FP is the total number of true OK samples. A low FRR is critical in manufacturing because it reduces unnecessary scrap/rework and stabilizes throughput, whereas accuracy alone can obscure this failure mode under class imbalance.

### 3.3. Experimental Results

As shown in Table 2, evaluation results of our capturing system are obtained. In terms of throughput, the average single-side tact time under continuous loading was 19.6 s, which corresponds to 39.2 s for dual-side inspection. This surpasses the 60 s/part criterion used in the performance evaluation and meets the stricter 40 s/part production goal reported for the 5-layer MEA line. Mechanical repeatability directly affects image stitching and AI robustness in a line-scan setup. For MEA, the inspection stage achieved  $\pm 7.68 \mu\text{m}$  position repeatability, and scan-axis driving deviation was within  $\pm 7 \mu\text{m}$ . Furthermore, transport damage was 0% in an external witnessed test, confirming that the loader–transfer–stage–unloader sequence can handle delicate MEA sheets without introducing cracks, folds, or other handling artifacts. The system’s optical and motion tuning yielded a defect detection limit of  $30.73 \mu\text{m}$  for MEA in the reported calibration. Combined with high-resolution acquisition and contrast-enhancing preprocessing, this enables identification of micro defects that are challenging for manual inspection.

Table 2. Summary of reported performance metrics for the PEMFC MEA capturing system.

Metric	Result (MEA)	Notes / Protocol
Dual-side tact time	39.2 s/part	Single-side 19.6 s averaged; dual-side computed by $\times 2$
Stage position repeatability	$\pm 7.68 \mu\text{m}$	Externally witnessed repeatability test
	$\pm 7 \mu\text{m}$	Drive deviation during y-axis scanning
Breakage rate	0%	No damage after repeated transport/handling tests
Defect detection limit	$30.73 \mu\text{m}$	Minimum recognizable defect scale in calibration

To evaluate the AI inspection system under production-relevant conditions, we trained the model using a curated dataset of 520 MEA images, split into 416 training images (222 OK, 194 NG) and 104 validation images (55 OK, 49 NG) as shown in Table 3. The labeling scheme comprised one OK class and seven defect categories—gasket bubble, gasket fold, electrode foreign particle, electrode fold/wrinkle, electrode discoloration, electrode pinhole, and eccentricity—to reflect the defect taxonomy targeted in this study. Furthermore, to calculate the FRR, 10 normal samples were prepared as a separate evaluation dataset. In particular, the dataset was acquired from an MEA manufacturing company over a four-month period in 2025, and the OK/NG labels were assigned by domain experts at the company

Table 3. Data set for PEMFC MEA AI inspection model.

Data Type	Defect Types	Number of data
Train	Normal type	222
	Defect types (gasket bubble, gasket fold, electrode foreign particle, electrode fold/wrinkle, electrode discoloration, electrode pinhole, and eccentricity)	194
Validation	Normal type	55
	Defect types (gasket bubble, gasket fold, electrode foreign particle, electrode fold/wrinkle, electrode discoloration, electrode pinhole, and eccentricity)	49

FRR	Normal type	10
-----	-------------	----

To classify OK and NG the surface in PEMFC MEAs, EfficientNetV2 were trained for 500 epochs with an input image size of 1000 and a batch size of 8 with the above dataset. The initial learning rate was set to  $1 \times 10^{-5}$ , and a warm-up strategy was applied for the first 5 epochs to stabilize training. Automatic mixed precision was not used, and the maximum number of detections was limited to 300. Training was conducted from scratch without resuming from a previous checkpoint, using four GPUs (devices 0, 1, 2, and 3) and four data-loading workers. To detect surface defects in PEMFC MEAs, this study compared YOLO11, YOLO12, and DETR. Because MEA defects vary widely in size, shape, contrast, and distribution, both the fast and practical YOLO models and the Transformer-based DETR were considered. Although YOLO11 and YOLO12 showed competitive detection performance with faster inference, DETR achieved better defect-type classification accuracy and was therefore selected as the final model. We trained the DETR under the same training settings as those used for EfficientNetV2. These results indicate that DETR can provide effective object detection performance for industrial images with complex defect shapes and distributions, such as those observed in MEAs. Figure 4 shows the training curves of the DETR-based defect detection model. Overall, the training losses, including giou loss, classification loss, and L1 loss, gradually decrease as the epochs increase, indicating that the model is learning the defect features effectively. The validation losses show some fluctuations but remain relatively stable, suggesting a reasonable generalization trend without severe divergence. In addition, the evaluation metrics, including precision, recall, mAP@0.5, and mAP@0.5:0.95, improve during training and then converge, demonstrating that the model progressively enhances its defect detection performance. Overall, these results indicate that the DETR model achieved stable learning behavior and satisfactory detection accuracy on the MEA defect dataset.

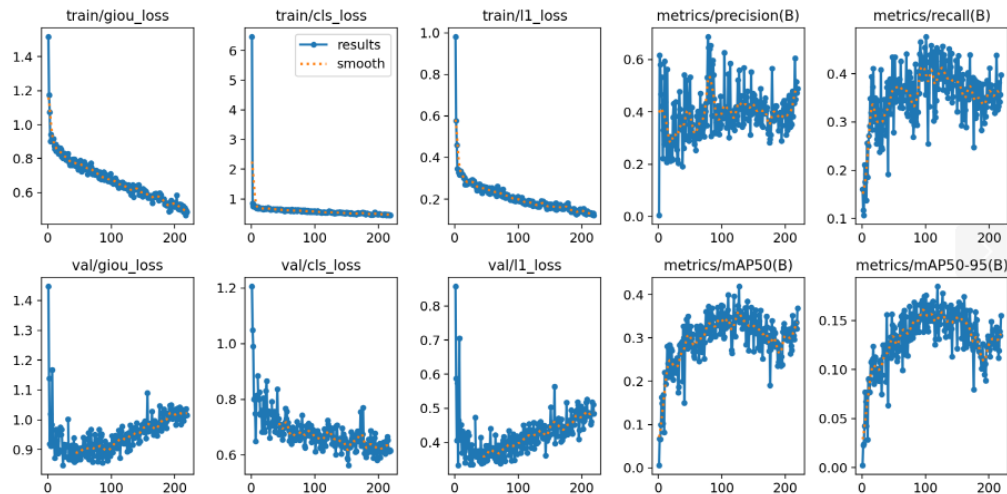


Figure 4. The training curves of the DETR-based defect detection model.

Figure 5 shows an example AI inspection overlay on a captured MEA image. Cyan bounding boxes mark localized anomaly detections, and the text (e.g., bad2 0.7, bad2 0.9) indicates the predicted defect class and its confidence score. Green labels (e.g., bad9 0.6) represent tile/ROI-level classification scores, summarizing whether a broader region is judged as defective. Presenting both classification (region-level) and detection (pixel-localized) outputs helps operators quickly verify where the defect is and how confident the system is, while supporting traceable OK/NG decisions under recipe-based thresholds. Figure 6 presents a qualitative comparison between the expert-annotated ground truth and the defect detection results obtained

by the DETR model for PEMFC MEA surface images. The left panel shows the defect regions and types labeled by domain experts, while the right panel shows the corresponding detection results predicted by the DETR model. Overall, the DETR model successfully identified the major defect regions and reproduced several defect categories with reasonable agreement with the expert annotations. In particular, prominent defects such as bubbles, pinholes, and discoloration were generally detected in similar locations. However, some discrepancies were also observed in small-scale or densely distributed defects, indicating that further improvement is still needed for fine-grained defect detection.

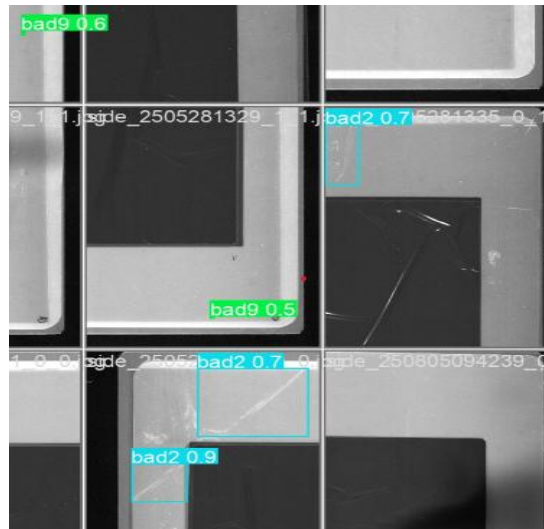


Figure 5. Example AI inspection overlay with predicted defect class and confidence.

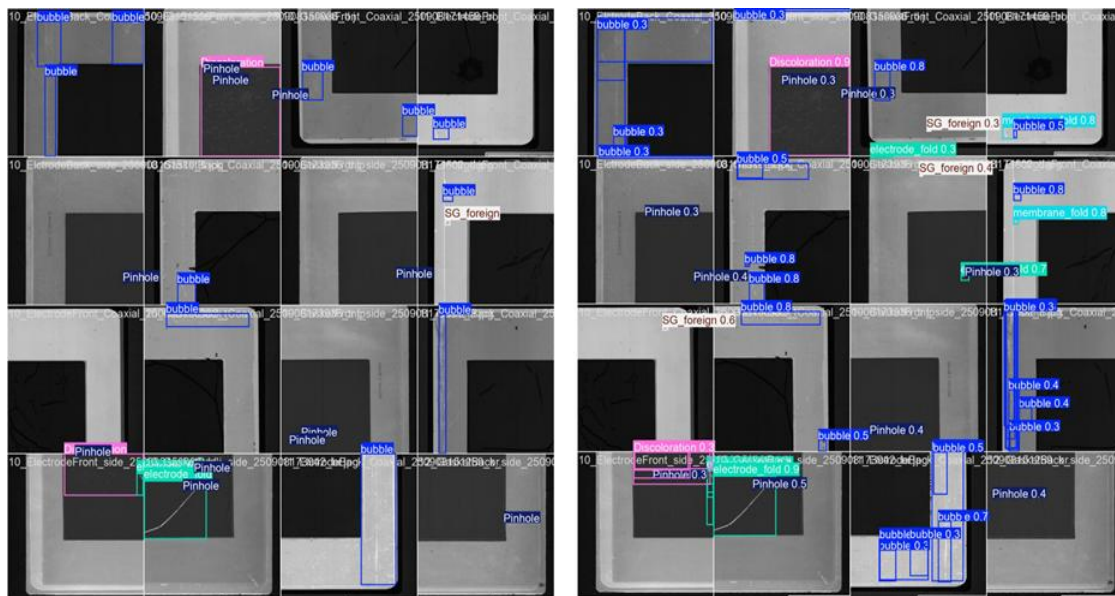


Figure 6. Comparison between expert annotations (left) and DETR-based defect detection results (right) for PEMFC MEA surface defects.

In this study, the final OK/NG decision was made hierarchically by combining classification and detection results. Samples classified as defective were directly judged as NG, whereas samples classified as normal were further verified using a detection model. If valid defect objects were

detected, the sample was classified as NG; otherwise, it was judged as OK. According to the strategy, the evaluation results indicate that the proposed AI inspection system delivers high decision reliability under production criteria while keeping unnecessary rejection of good parts very low. As shown in Table 4, the system achieved an overall accuracy of 97.11%, meaning that nearly all inspection decisions matched the ground-truth labels when the same customer-defined acceptance rules (recipe thresholds for size/tolerance) were applied. In practice, this level of accuracy suggests stable discrimination between OK and NG outcomes in a production-like setting, where the final judgment is governed not only by model scores but also by pass and fail criteria aligned with the line. More importantly from a manufacturing standpoint, the system exhibited a false reject rate (FRR) of 0.99% on OK parts, measured over 200 repeated runs (10 OK parts  $\times$  20 repeats). This result implies that only about 1 out of 100 OK decisions would be incorrectly rejected as NG under repeated operation, which directly translates to minimal yield loss and reduced rework/scrap attributable to the inspection system. Overall, the combined results—97.11% accuracy and 0.99% false reject rate—show that the inspection system maintains strong agreement with ground truth while remaining production-friendly, i.e., it does not introduce significant throughput penalties or yield degradation due to excessive false alarms on OK parts.

Table 4. Summary of reported performance metrics for the PEMFC MEA AI inspection.

Metric	Result (MEA)	Notes / Protocol
Accuracy	97.11%	Evaluation against ground truth under production criteria
False reject rate (FRR)	0.99%	200 runs (10 OK parts $\times$ 20 repeats); Non-detection = 1 - Recall

#### 4. CONCLUDING REMARKS

The reported results indicate that a combined approach—mechanically stable line-scan imaging paired with an AI pipeline that balances classification speed and detection precision—can meet the requirements of MEA mass production. Automated loading with interleaving-paper handling reduces operator burden while preserving part integrity, and the vacuum stage mitigates warping that would otherwise confound edge- and texture-based defect cues.

From an AI perspective, quadrant-based inspection is a practical compromise between resolution and compute cost. Beyond memory savings, tiling helps re-scale micro defects to a larger portion of the input, improving detectability. Nevertheless, DETR results suggest that very small defects remain challenging, and further gains may require multi-scale feature fusion, improved labeling consistency for rare classes, and active learning loops that prioritize hard examples.

Operationally, low non-detection (false reject) is critical because false rejects can disrupt line flow and increase rework. Achieving sub-1% non-detection while maintaining <40 s dual-side tact time demonstrates that the proposed system can be integrated without becoming a bottleneck. Future work should extend evaluation to longer-term drift, including illumination aging, sensor contamination, and domain shifts across MEA variants.

This paper presented a production-oriented PEMFC MEA inspection system that integrates automated feeding, dual-side line-scan imaging, and an AI pipeline combining EfficientNetV2 classification with DETR detection. Using a high-resolution dataset and a quadrant-based tiling strategy, the system achieved 97.11% agreement, 0.99% non-detection rate for conforming parts, and 39.2 s tact time for dual-side inspection, while maintaining micrometer-level motion repeatability and zero handling damage. These results support practical deployment for MEA

mass production and provide a reference architecture for high-throughput inspection of flexible electrochemical components.

## ACKNOWLEDGEMENTS

This work was supported by the Korea Institute of Energy Technology Evaluation and Planning(KETEP) and the Ministry of Trade, Industry & Energy(MOTIE) of the Republic of Korea (No. RS-2024-00419270).

## REFERENCES

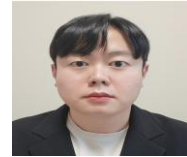
- [1] Z. Wang *et al.*, “Application progress of small-scale proton exchange membrane fuel cell,” *Energy Reviews*, vol. 2, no. 2, Jun. 2023, 100017, doi: 10.1016/j.enrev.2023.100017.
- [2] D. Wheeler and G. Sverdrup, “2007 Status of Manufacturing: Polymer Electrolyte Membrane (PEM) Fuel Cells,” NREL Tech. Rep. NREL/TP-560-41655, Mar. 2008.
- [3] M. Grandi *et al.*, “Recent advancements in high performance polymer electrolyte fuel cell electrode fabrication – Novel materials and manufacturing processes,” *Journal of Power Sources*, vol. 562, Apr. 2023, 232734, doi: 10.1016/j.jpowsour.2023.232734.
- [4] M. Wang *et al.*, “Manufacturing-induced irregularities of membrane electrode assemblies: Impacts on poly exchange membrane fuel cells’ performance and diagnosis,” *Renewable and Sustainable Energy Reviews*, vol. 216, Jul. 2025, 115707, doi: 10.1016/j.rser.2025.115707.
- [5] S. Mauger, “Membrane Electrode Assembly Manufacturing Automation Technology for the Electrochemical Compression of Hydrogen: Cooperative Research and Development Final Report (CRADA CRD-18-00744),” NREL Tech. Rep. NREL/TP-5900-95403, Aug. 2025.
- [6] K. Zuiderveld, “Contrast Limited Adaptive Histogram Equalization,” in *Graphics Gems IV*, P. S. Heckbert, Ed. Academic Press, 1994, pp. 474–485.
- [7] P. Soille, *Morphological Image Analysis: Principles and Applications*, 2nd ed. Springer, 2004, doi: 10.1007/978-3-662-05088-0.
- [8] R. Szeliski, *Computer Vision: Algorithms and Applications*. Springer, 2010, doi: 10.1007/978-1-84882-935-0.
- [9] M. Tan and Q. V. Le, “EfficientNetV2: Smaller Models and Faster Training,” in *Proc. 38th Int. Conf. Machine Learning (ICML)*, PMLR, vol. 139, pp. 4103–4115, 2021.
- [10] A. Krizhevsky, I. Sutskever, and G. E. Hinton, “ImageNet Classification with Deep Convolutional Neural Networks,” *Communications of the ACM*, vol. 60, no. 6, pp. 84–90, 2017, doi: 10.1145/3065386.
- [11] A. Voulodimos, N. Doulamis, A. Doulamis, and E. Protopapadakis, “Deep Learning for Computer Vision: A Brief Review,” *Computational Intelligence and Neuroscience*, vol. 2018, Article ID 7068349, 2018, doi: 10.1155/2018/7068349.
- [12] N. Carion, F. Massa, G. Synnaeve, N. Usunier, A. Kirillov, and S. Zagoruyko, “End-to-End Object Detection with Transformers,” in *Computer Vision – ECCV 2020*, LNCS, vol. 12346, pp. 213–229, Springer, 2020, doi: 10.1007/978-3-030-58452-8\_13.
- [13] S. Ren, K. He, R. Girshick, and J. Sun, “Faster R-CNN: Towards Real-Time Object Detection with Region Proposal Networks,” *IEEE Trans. Pattern Anal. Mach. Intell.*, vol. 39, no. 6, pp. 1137–1149, Jun. 2017, doi: 10.1109/TPAMI.2016.2577031.
- [14] T.-Y. Lin *et al.*, “Microsoft COCO: Common Objects in Context,” in *Computer Vision – ECCV 2014*, LNCS, vol. 8693, pp. 740–755, Springer, 2014, doi: 10.1007/978-3-319-10602-1\_48.
- [15] L. Bottou, F. E. Curtis, and J. Nocedal, “Optimization Methods for Large-Scale Machine Learning,” *SIAM Review*, vol. 60, no. 2, pp. 223–311, 2018, doi: 10.1137/16M1080173.

**AUTHORS**

**In Joo** received the B.S. degree and the M.S degree in Computer Science from Chungbuk National University in Korea in 2021 and 2023, respectively. He is currently pursuing his PhD in Computer Science at the same university. His research interests include computer vision and deep learning techniques, as well as Big Data analysis.



**Kyeongtae Son** received the M.S. degree in Electronic Engineering from Korea National University of Transportation in Korea in 2015. He is currently with LAT Co., Ltd., where he conducts R&D in vacuum and plasma technology and is involved in research on integrating artificial intelligence (AI) into the fields.



**Yong-Seong Kim** receives the Ph.D. in Electronic Engineering from Cheongju University in 2006. He is currently with LAT Co., Ltd., where he conducts R&D in vacuum and plasma technology and is involved in research on integrating artificial intelligence (AI) into the fields.



**Ga-Ae Ryu** received the B.S. degree in cyber investigation major from Gwangju University, South Korea, in 2014, and the M.S. degree in digital information convergence and the Ph.D. degree in computer science from Chungbuk National University, South Korea, in 2016 and 2022, respectively. She is currently a Senior Researcher with the Department of AI Convergence Research Division, Korea Institute of Ceramic Engineering and Technology. Her research interests include AI-based materials analysis, computer vision, digital twin, smart factory application, and big data platform.



**Kwan-Hee Yoo** works as a professor at the Department of Computer Science at Chungbuk National University, Korea. He received his B.S. in Computer Science from the same university in 1985 and his M.S. and Ph.D. in Computer Science from KAIST (Korea Advanced Institute of Science and Technology), Korea, in 1988 and 1995, respectively. His research interests include AI-based computer vision, computer graphics, 3D character animation, and dental/medical applications.

